Icarus 411 (2024) 115942

Contents lists available at ScienceDirect

Icarus

journal homepage: www.elsevier.com/locate/icarus

Research Paper

Possibly seismically triggered avalanches after the S1222a Marsquake and S1000a impact event

A. Lucas [a,*], I.J. Daubar [b], M. Le Teuff [a], C. Perrin [c], T. Kawamura [a], L. Posiolova [d], P. Lognonné [a], S. Rodriguez [a], D. Giardini [e], G. Sainton [a], A. Mangeney [a], A. McEwen [f]

[a] Université Paris Cité, Institut de physique du globe de Paris, CNRS, F-75005, Paris, France
[b] Brown University, Providence, RI, USA
[c] Nantes Université, Université d'Angers, Le Mans Université, CNRS, UMR 6112, Laboratoire de Planétologie et Géosciences, UAR 3281, Observatoire des Sciences de l'Univers de Nantes Atlantique, Nantes, France
[d] Malin Space Science System, San Diego, CA, USA
[e] ETH, Zurich, Switzerland
[f] U. Arizona, USA

ARTICLE INFO

Keywords:
Mars
Seismic event
Dust avalanche
Impact crater

ABSTRACT

Ground motion from seismic events detected by the SEIS/InSight seismometer on Mars could potentially trigger dust avalanches. Our research strongly suggests that the seismic event S1000a may have triggered a significant number of dust avalanches. In contrast, following the seismic event S1222a, there was only a modest increase in avalanche occurrences. Orbital observations of the area surrounding the projected location of the S1222a quake reveal notable topographic features, such as North-South ridges and impact craters. We utilize orbital imagery to evaluate the rate of avalanches and explore how the S1222a event might have influenced this rate. The S1222a event appears to be a plausible factor contributing to the observed increase in avalanches. Our further analysis of the epicenter location aims to clarify how it aligns with the avalanches' spatial distribution, offering insights into the regional topography.

Plain language summary

We explore the potential effects of seismic aftermath on Mars, focusing on how large seismic events might trigger dust avalanches and mass wasting. Our analysis of orbital data reveals that the affected area is characterized by steep slopes, predominantly around crater walls, where dust accumulation is substantial. This geological setup makes the region particularly prone to dust avalanches. Large seismic events are known to cause ground acceleration, which can reduce material cohesion and friction, or increase tangential strain. These changes are conducive to mass wasting. Based on our research, we propose that the S1222a marsquake could be a primary factor contributing to the observed increase in avalanche activity, as evidenced by our analysis of orbital imagery. This finding sheds light on the dynamic interplay between seismic activity and surface processes on Mars.

1. Introduction

On May 4, 2022, a major seismic event named S1222a (Kawamura et al., 2023) was recorded by the SEIS instrument (Lognonné et al., 2019) of the InSight mission (Banerdt et al., 2020). It was an unprecedented marsquake in the SEIS recording period with an estimated moment magnitude of M_W^{Ma} 4.7 (InSight Marsquake Service, 2022). In comparison, 95% of events recorded by SEIS since landing in November 2018 had a magnitude below 3.5 (Clinton et al., 2021; Böse et al., 2021; Ceylan et al., 2022; Knapmeyer et al., 2023). As for some of the InSight events, a location was estimated with a back-Azimuth (bearing from the event toward InSight) of 101° (96°-112°) and an epicentral distance Δ = 37° (±1.6°) which places the event epicenter at the location of 3.0°S,171.9°E (Kawamura et al., 2023) (green star on Fig. 1). Other nearby locations for the epicenter have also been proposed (Panning et al., 2023; Kim et al., 2022) (Fig. 1). No new impact crater has been reported that could be the source of this event (Fernando et al., 2023). The region shows many topographic features including a few tectonic structures expressed as north-south wrinkle ridges (Knapmeyer et al., 2006) and impact craters (Fig. 1). To the east of this region, the only major structures are Appollinaris Patera, a Noachian volcano (Tanaka et al., 2014) about 200 km in diameter, and a large alluvial fan spanning southwards from the volcano's rim.

* Corresponding author.
E-mail address: lucas@ipgp.fr (A. Lucas).

https://doi.org/10.1016/j.icarus.2023.115942
Received 12 November 2023; Received in revised form 20 December 2023; Accepted 28 December 2023
Available online 4 January 2024

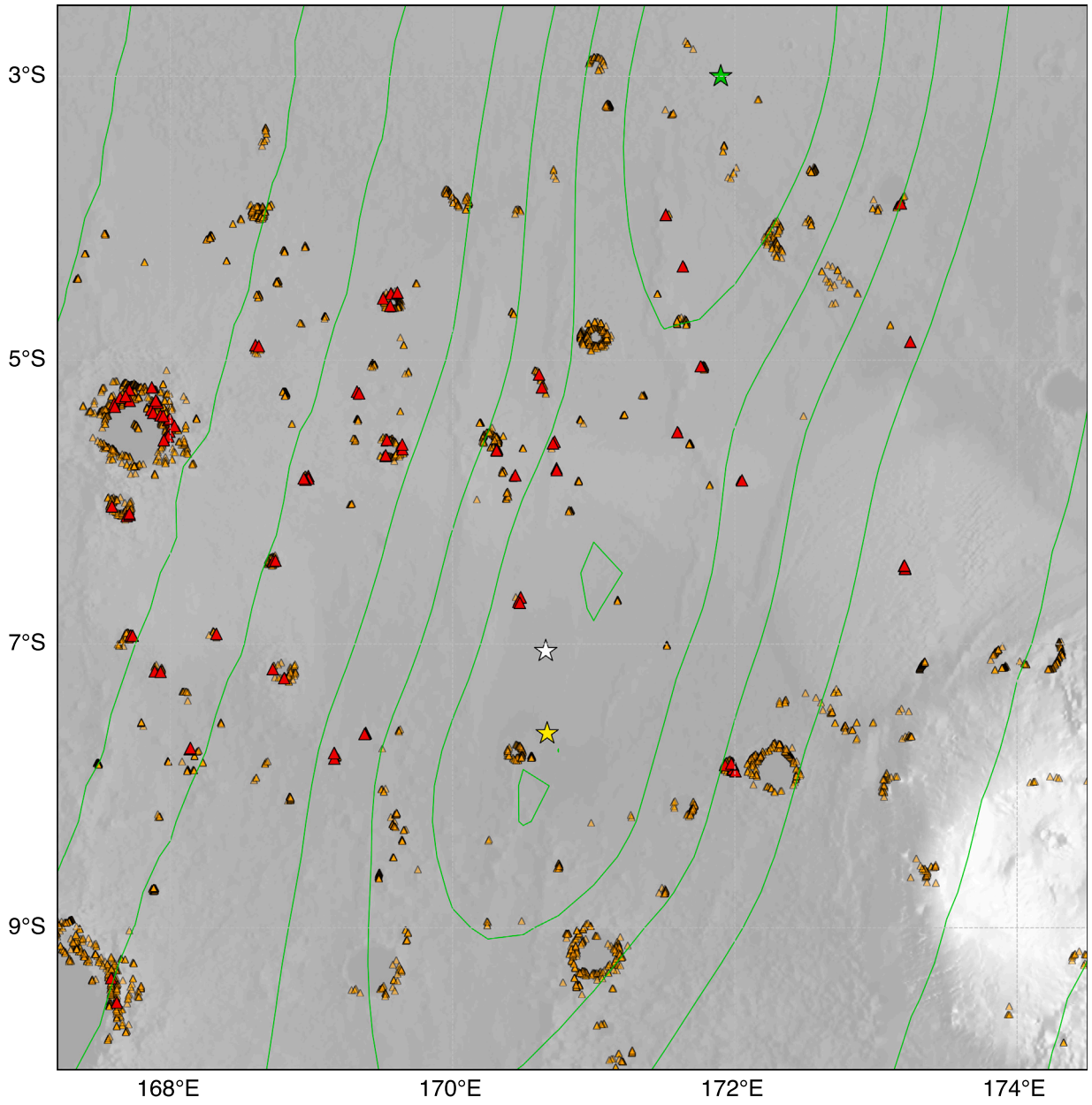

Fig. 1. Regional map of dust avalanches near the S1222a event estimated location (green star with associated green contours, (Kawamura et al., 2023). The white star is the location estimated by multi-orbit surface waves (Panning et al., 2023). The yellow star shows the estimated location according to surface waves (Kim et al., 2022). Orange symbols are all avalanches mapped. Red symbols show where avalanches are observed on post-event images. Basemap is the MOLA elevation map (Smith et al., 2001). (For interpretation of the references to color in this figure legend, the reader is referred to the web version of this article.)

From orbital images, we identified dust avalanches (also known as slope streaks) in this region (orange symbols on Fig. 1). These are known active mass wasting processes occurring on Mars in several contexts (Ferguson and Lucchitta, 1984; Sullivan et al., 2001; Aharonson et al., 2003; Schorghofer et al., 2002, 2007; Schorghofer and King, 2011; Gerstell et al., 2004; Baratoux et al., 2006; Chuang et al., 2007; Bergonio et al., 2013; Heyer et al., 2019, 2020; Valantinas et al., 2021). They appear as relatively dark or bright streaks on steep dust-covered slopes and occur in regions with a high albedo and low to very low thermal inertia (Sullivan et al., 2001; Aharonson et al., 2003). Dust avalanches on Mars typically appear darker than the surrounding terrain. This is likely due to the removal of lighter-colored surface dust by the avalanches. When a slope streak is formed, loose dust and sand on the surface are mobilized and cascade down the slope, exposing the darker, underlying material (Malin et al., 2007; Dundas, 2020). This material may be darker due to several factors, such as the presence of iron-rich minerals or alteration by weathering processes (Christensen et al., 2001). In addition, the removal of surface dust by the avalanches may expose a rougher, more textured surface, which can scatter and absorb more light, making the streak appear even darker. Many studies discuss possible triggering conditions and emplacement mechanisms. Purely dry avalanches of fine dust have been explored from the perspective of both observations (Schorghofer et al., 2007; Phillips et al., 2007; Dundas, 2020), and numerical simulations (Lucas, 2010). Spring discharge involving salty groundwater and/or brines in the shallow subsurface has been proposed (Ferris et al., 2002; Miyamoto, 2004; Head et al., 2007; Kreslavsky and Head, 2009; Bhardwaj et al., 2017, 2019). Other possible triggers include wind (Baratoux et al., 2006; Heyer et al., 2019), seismic activity from impacts or internal forces, or boulder track (Chuang et al., 2007) have been proposed.

While previous studies looked at boulder falls and associated tracks triggered by possible paleo-seismic activity (Roberts et al., 2012; Brown

and Roberts, 2019), no previous work could have directly tested the possibility of seismically induced mass wasting on Mars due to a lack of seismic event records before the InSight mission. In the framework of the recent seismic events S1000a and S1222a, we investigate the effects of the induced ground acceleration aftermaths as a potential triggering mechanism for dust avalanches in the vicinity of the located epicenter. To do so, we conduct regional mapping of the avalanches from pre-event and post-event imagery in order to estimate the effect of the marsquake and impact crater on the rate of avalanches. We take into account possible biases due to the limited number of images, the time span between images, the sub-surface properties through thermal behavior, and the various sensitivities of each camera sensor.

2. Methods

2.1. Orbital data and mapping

As soon as the S1222a event was detected by SEIS and an estimate of the epicenter location was provided, we investigated orbital observations provided by the Context (CTX) and High Resolution Imaging Science Experiment (HiRISE) cameras (Malin et al., 2007; McEwen et al., 2007), both on board the Mars Reconnaissance Orbiter (MRO). Along with MRO imagery, we examine images from the Mars Global Surveyor (MGS)/Mars Orbiter Camera (MOC) (Malin et al., 1992), and THEMIS-Vis/Odyssey (Fergason et al., 2006). This led to a set of hundreds of images acquired before the seismic event. In addition, we requested new MRO observation over areas where we mapped avalanches inside the uncertainty area (Kawamura et al., 2023) (Fig. 1, Supp. Info text S1). At the time of writing this paper, a dozen HiRISE images and thirty new CTX observations were obtained, all acquired after the S1222a seismic event. In addition to imagery, we used Digital Terrain Models (DTMs) from both Mars Orbiter Laser Altimeter (MOLA, Smith et al. (2001)) and High Resolution Stereo Camera (HRSC, Neukum and Jaumann (2004)), the geological map from Tanaka et al. (2014) and the thermal inertia map (Christensen et al., 2004) (See Supp. Info. Text S2), which all provide contextual information. Note that Fig. 1 specifically depicts the area covered by post-S1222a event CTX imagery. All the data have been combined into a Geographical Information System (GIS) in order to manually map all avalanches in the region of interest (Fig. 1), by two independent people (see Supp. Info. Text S1 for details on the imagery processing and mapping). The older observations, provided by both MOC and THEMIS-Vis, were only used for confirming the very low fading rate (Sullivan et al., 2001), being in good agreement with the dust activity reported in this region (Battalio and Wang, 2021).

2.2. Estimates of avalanche rate and statistics

Avalanche rate q is obtained from equation provided in Aharonson et al. (2003):

$$q = 100 \times \frac{\Delta n}{n \Delta t}, \quad (1)$$

where n is the total number of avalanches observed in both the two overlapping images, Δn being the newly observed avalanches on the recent image and not in the older image, and Δt being the time span between the two observations in Martian years. This rate q is expressed in % of new events/Martian year (Aharonson et al., 2003). This method has also been used by recent work (Heyer et al., 2019). The time periods between overlapping images in our database range from ~0.3 to almost 7 martian years.

Finally we agglomerate avalanches in the same location (i.e. crater) and hence to compute the avalanche rate in each area where new events can be observed between two overlapping images. As opposed to a squared binning, hexagons are more similar to circles, hence they better translate data aggregation around the bin center. As most areas covered by avalanches in this region are impact craters, this provides a more valuable way to decipher the avalanche coverage.

3. Results and discussion

3.1. Avalanches triggered after S1000a impact event

Before discussing S1222a event, we investigated S1000a impact event which occurred on September 18 2021, and left a crater over 150 m in diameter at 38.1°N;-79.87°E (Fig. 2). This event was recorded by SEIS and then orbital imagery revealed its actual location. Its magnitude was estimated to be around M_w^{Ma} 4.1, hence about 25 times smaller that S1222a in energy (Ceylan et al., 2022; Posiolova et al., 2022). It should be noted that the location estimate from the seismic signal analysis was felt at approximately 130 km away from the actual location, as discussed in Posiolova et al. (2022). By analyzing all pre-event images including CTX, and HRSC and post-event HiRISE images, we could map a very large number of avalanches not seen in pre-event imagery. By looking back in time using all available images, including MOC/MGS, we observed that these areas were not covered by dust avalanches prior to the impact event (Fig. 2.).

We looked at the density distribution of the new avalanches (as seen on the post-event images and having the same brightness, hence the same age) as a function of their respective distance to the impact crater (histogram inset in Fig. 2). This distribution follows a bell-shaped curve. As seen on Earth, seismically triggered mass-wasting is absent very close to the epicenter, and increases at farther distances until it decreases again at the farthest distances (e.g., Tatard, 2010; Livio and Ferrario, 2020). Nonetheless, the mechanism here is different. It is very likely that the avalanches are triggered by secondary impacts, and not seismic waves. As an example of a typical scenario, ejecta leaving the primary impact at a velocity v = 200 m s^{-1}, with a launch angle of θ = 45°, will have a ballistic flight time t_f of 76 s (i.e., $t_f = 2 \times v \sin\theta / g$), and will land at a distance d_l = 10.78 km (neglecting the air friction, $d_l = v \cos\theta \times t_f$). Hence, the histogram in the inset of Fig. 2 is similar to the statistical distribution of secondary ejecta impacting the ground. This correlation indicates those secondary impacts are a likely source for the avalanches. Of course, the S1000a event is an ideal case. First of all, we know the position of the epicenter perfectly well, thanks to the orbital imagery revealing the source crater. What is more, the presence of northeast-southwest trending ripples implies the presence of uniformly distributed topographic slopes as moving away from the impact crater, hence the avalanche susceptibility. Note that Burleigh et al. (2012) demonstrated that impact blast can trigger slope streaks. The S1000a event also shows that an impact with a seismic magnitude M_w^{Ma} 4.1 can trigger a very large number of avalanches on Mars. As such, this is likely be discussed more thoroughly in a following work which would evaluate the ballistic recomposition in order to evaluate potential effects of secondary impacts on the dust avalanche triggering. However, the ground accelerations caused by a surface impact and a deep earthquake are not the same. So, in view of our results for the S1000a event, we discuss our results for S1222a in the following sections.

3.2. Avalanche rate increase in post-marsquake S1222a images

We analyzed all image pairs over the whole area of interest near the S1222a estimated epicenter. We identified 4532 avalanches (orange symbols in Fig. 1). More than 200 avalanches were identified on pre-event images (over the 2005–2021 period), and 122 were identified on the post-event CTX images with respect to their 2005–2021 period counterparts respectively. An example is given in Fig. 3-a. Note that, while doubtful avalanches may have been detected (e.g., yellow symbols in Fig. 3-a), we only took into account the robust observations of new avalanches (e.g., red symbols in Fig. 3-a). For the statistical robustness, we then derived avalanche rates q for each CTX/CTX pair only. When times series were available, we derived avalanche rate chronicles (Fig. 3-b). As exemplified on Fig. 3-b, a strong increase of q is observed after the S1222a event. Indeed, over the whole area of

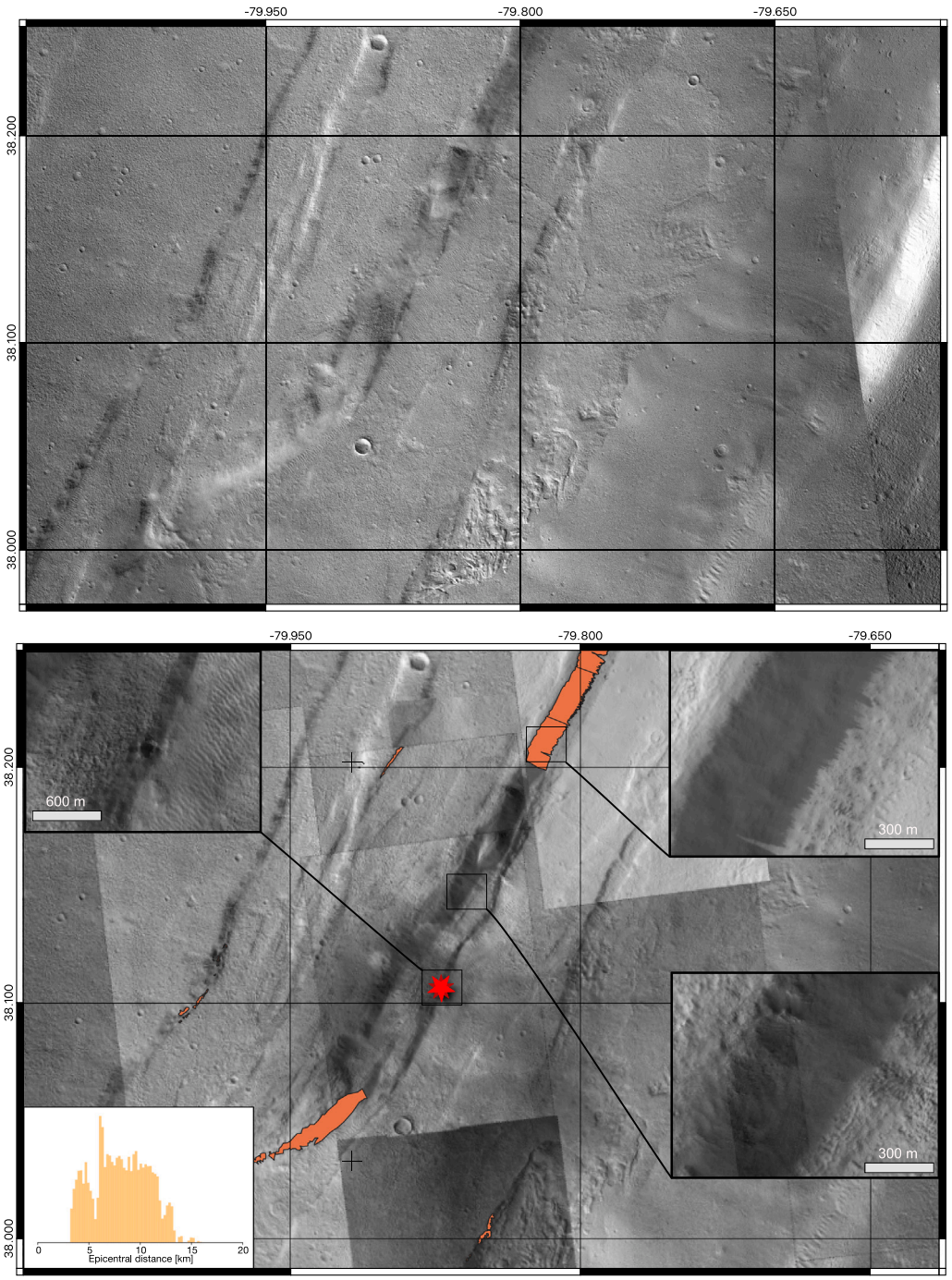

Fig. 2. (top) Pre-event CTX mosaic around the impact location of S1000a (dated from 2018-09-12) showing absence of any dust avalanches. (bottom) Post-event HiRISE mosaic on top of CTX images around the impact location of S1000a event (red star) with associated triggered avalanches (orange areas). Insets show close-up on the crater, the avalanches areas and slopes without new avalanches (from top-left, to bottom-right, respectively). The density distribution of avalanches with respect to the epicentral distance is shown in the bottom-left inset. (For interpretation of the references to color in this figure legend, the reader is referred to the web version of this article.)

interest (Fig. 1), the pre-event rates (circles in Fig. 3-c) lie around 2.6%.MYear^{-1} with a maximum value of 6%.MYear^{-1}, accounting for uncertainties following Aharonson et al. (2003). These values are in agreement with in previous estimated by Aharonson et al. (2003), and avalanche rates do not differ substantially across the region covered by our study. In contrast, post-event values of q show a significantly different distribution both spatially and in amplitude (Fig. 3-c,d). While most rates still fall below 10%, we observe that in 9 places, the rates are >10%, as high as 40% (excluding outlier, Fig. 3-d). If we keep only the sub-10% values, the average is the same as that before the seismic event (2.6%.MYear^{-1}), and there is also no dependence on the epicentral distance. Interestingly, the highest post-event q (>20%) are found at the smallest distances from the epicenter of the S1222a event proposed by Kawamura et al. (2023). When relating the derived avalanche rate q to the epicentral distance Δ with respect to the estimated location from Kawamura et al. (2023), we obtained a slight decreasing trend of q with Δ. Finally we also verified that temporal sampling of the orbital images (Δt) does not bias the avalanche rate estimates (Fig. 3-e).

To address the limited number of observations, we employed a permutation test, also known as bootstrapping (Efron and Tibshirani, 1993; Davison and Hinkley, 1997). This non-parametric approach does not rely on specific distribution assumptions about the data. We began

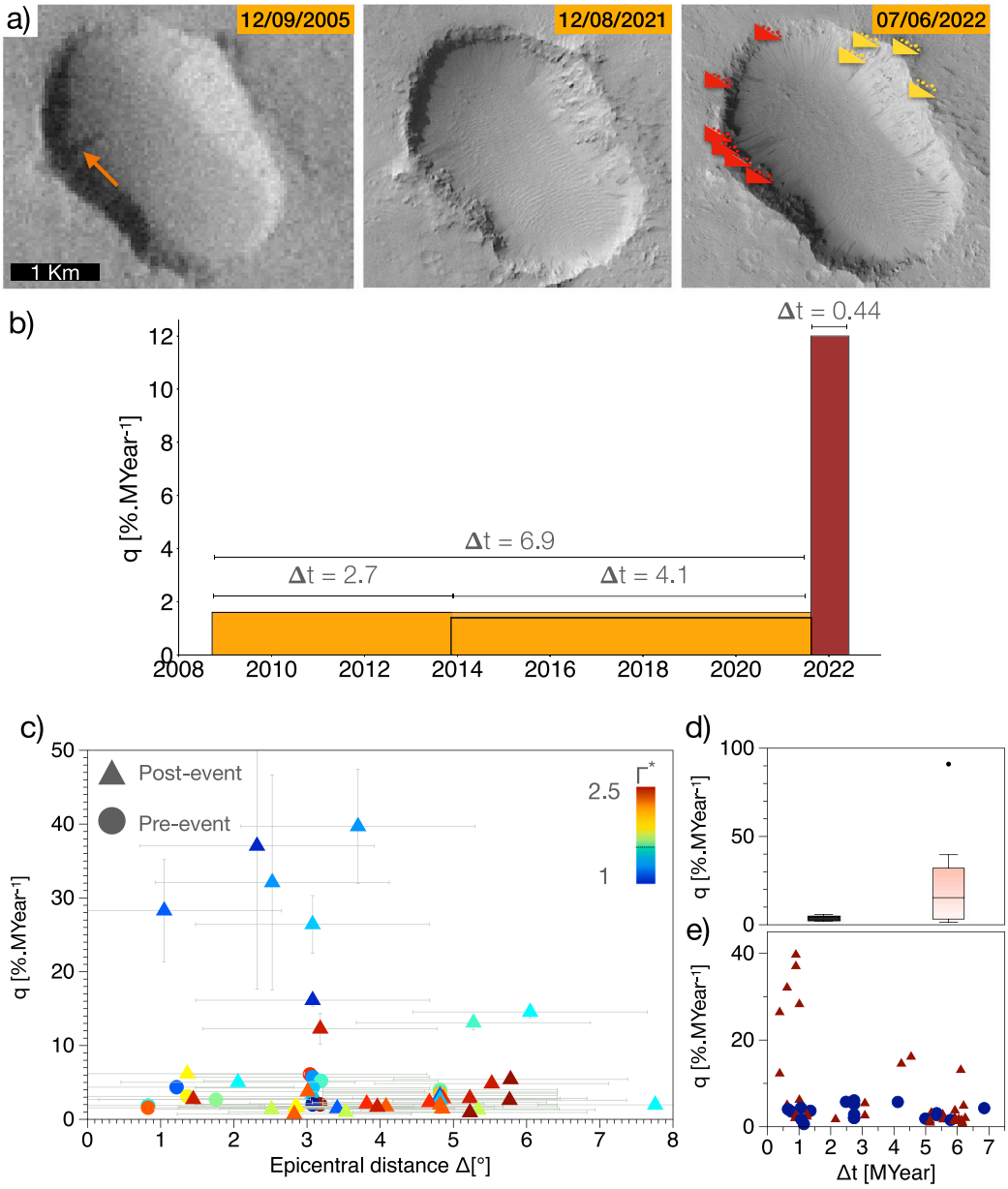

Fig. 3. (a) Image times series with THEMIS-Vis image V1768100 (17m/pixel) taken in 2005, CTX image N21_070520_1744_XI_05S189 W (6m/pixel) taken 8 months before S1222a, and an HiRISE image (downsampled to 5m/pixel) ESP_074357_1745 taken a few weeks after the marsquake. New avalanches marked with the red symbols. Additional doubtful avalanches are indicated with the yellow symbols, (b) time series of avalanche rate q over the 2008–2022 period (orange for pre-event period, red for image pair including post-event observations). (c) Avalanche rate q as a function of the epicentral distance Δ (with respect to the green star of Fig. 1) for CTX/CTX image pairs. Symbols are associated to pre-event (circles) or post-event (triangles). Color scales with the ratio of apparent thermal inertia (Γ^*, with dashed line at 1.5). (d) Box plot of avalanche rates for pre-event pairs (black) and pre/post-event pairs (red). (e) Avalanche rate q as a function of timespan Δt. Note that some symbols can overlap each other on both plots. (For interpretation of the references to color in this figure legend, the reader is referred to the web version of this article.)

by calculating the avalanche rate for each CTX/CTX pair for both pre-event and post-event observations, determining the mean difference as our observed statistic. Then, we merged the pre-event and post-event rates, treating them as a combined dataset without distinction of their original times. This pooled data was randomly shuffled to create new groups, preserving the original group sizes. We calculated the permuted test statistic by assessing the avalanche rate in this permuted data. This permutation process was iterated a million times, generating a distribution of test statistics under the hypothesis of no marsquake influence. Comparing our observed statistic to the 95% confidence interval derived from bootstrapping, we found that the post-event avalanche rates in all CTX observations exceeded 95% of the bootstrap statistic distribution. This indicates a significant increase in avalanche activity following the seismic event. However, it is important to note that the area studied includes locations possibly too distant from the epicenter to be affected by the marsquake. Focusing on rates exceeding 6%.MYear^{-1}, the post-marsquake rates surpassed the 99.98% confidence level. These findings, along with the detailed bootstrapping procedure, are outlined in Algorithm 1 and illustrated in Fig. 4.

3.3. Effect of the relative thermal inertia

Subsurface properties at shallow depths can be analyzed through thermal inertia, which indicates how solar energy absorption and subsequent subsurface heat propagation relate to material properties. Thermal inertia is represented as $\Gamma \equiv \sqrt{\kappa_e(1-p)\rho C(T)}$, where κ_e denotes

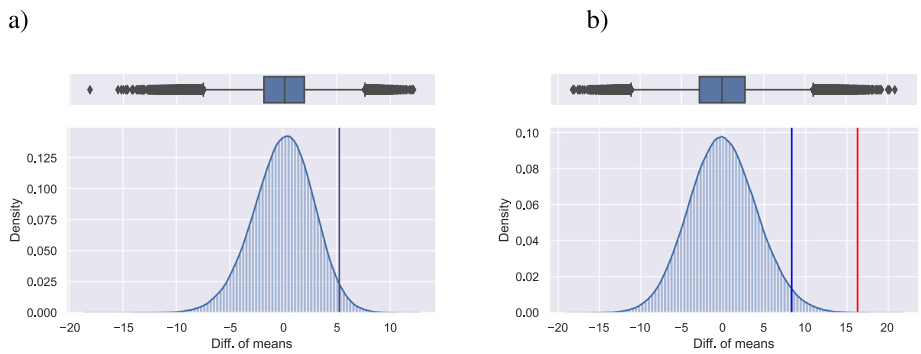

Fig. 4. Bootstrapping statistics. (a) accounting for the whole data set, (b) when only considering q> 5 for the post-event observation. (top-panel) Quantiles of the permutation tests. (bottom-panel) The distribution of the permutation tests. The thin vertical blue lines gives the 95% of the test statistics distribution. The dashed red vertical line shows the observed statistics. (For interpretation of the references to color in this figure legend, the reader is referred to the web version of this article.)

Algorithm 1: Assessing Influence of marsquake on avalanche rate

Input: Pre-event image pairs $(n, \Delta n, \Delta t)$

Input: Post-event image pairs $(n, \Delta n, \Delta t)$

Define the observed test statistic: Δn_{obs} (change in the number of avalanches), n_{obs} (number of avalanches), and Δt_{obs} (time difference between images);

Combine the before and after data into a single pool, disregarding their original labels;

Perform resampling with replacement: Randomly sample, with replacement, from the pooled data to create a bootstrap sample of the same size as the original data set. Repeat this process to generate a large number of bootstrap samples.

Calculate the test statistic for each bootstrap sample: Compute the rate of avalanches for each bootstrap sample, given by $\frac{\Delta n_{boot}}{n_{boot}\Delta t_{boot}}$.;

Calculate the bootstrap statistic distribution: Collect the calculated test statistics from step 4 to form the bootstrap distribution of the test statistic;

Calculate the confidence interval: Determine the desired confidence level (e.g., 95%). Compute the lower and upper percentiles of the bootstrap distribution corresponding to the chosen confidence level;

Output: Assessment of marsquake influence

effective thermal conductivity, p is porosity, ρ represents density, and $C(T)$ is the specific heat capacity. Therefore, low thermal inertia can indicate high porosity, low density, small grain size, or a combination of these factors. As Sullivan et al. (2001) and Aharonson et al. (2003) previously demonstrated, dust avalanches on Mars typically occur on steep slopes and are found in areas with low absolute thermal inertia. It is important to note that thermal inertia values are derived from models and assumptions, as detailed by Christensen et al. (2004). Due to significant variations between orbits, we calculate the ratio of the apparent value of thermal inertia at avalanche scar location with respect to the median value on the surrounding plains, and named hereafter $\Gamma^* = \Gamma_{avalanche}/\Gamma_{plain}$ (see Supp. Info. Text S2). By examining Γ^*, we found that areas with the lowest values experience the most significant increases in avalanche rates (see Fig. 3-c). Specifically, when $\Gamma^* \gg 1.5$, post-event avalanche rates do not exceed pre-event rates. Conversely, an increase in q is observed when $\Gamma^* < 1.5$ This leads us to conclude that post-event avalanche susceptibility on Mars is primarily influenced by scarp locations with steep slopes and the lowest apparent thermal inertia. Such conditions correspond to the most unconsolidated terrains or areas with fine granular material.

3.4. Epicentral distance and possible sources of the quake

Although the epicentral distance is far from being the only parameter that controls the avalanche rates, it remains an important control factor (Tatard, 2010; Livio and Ferrario, 2020) (Supp. Info. Text S3 and S5). The reason is that the transition between a static state and a flowing state is modeled by introducing a threshold allowing the material to flow. This has been shown to quantitatively capture debris and rock avalanche morphodynamics on Mars (Lucas, 2010; Lucas and Mangeney, 2007; Lucas et al., 2011, 2014) (see Supp. Info. Text S3). Nonetheless, local geology, fractures, aftershocks and historical events will have a significant effect on the aftermaths of an earthquake by leading the slopes close to failure (Tatard, 2010; Livio and Ferrario, 2020; Chen et al., 2020; Rosser et al., 2021; Lombardo and Tanyas, 2022). Taking into account all these considerations, the rate would not be expected to be controlled only by epicentral distance. However, our constraints on the characteristics of the marsquake are weak, especially in terms of depth, focal mechanisms, and therefore the resulting ground acceleration. Our knowledge on the geological heterogeneity is also poorly constrained. Also, compared to terrestrial standards, this marsquake remains a small event. Nonetheless, small seismic events have shown to significantly increase the rate of landslides on Earth (Martino et al., 2022). Indeed, recent studies show that even very small amplitude seismicity may trigger instabilities on metastable slopes (Bontemps et al., 2020; Durand et al., 2023).

Nonetheless, under the hypothesis that event S1222a did trigger avalanches, we considered the empirical model proposed by Livio and Ferrario (2020) which relates the distribution of triggered avalanches N_{ava} with the epicentral distance Δ:

$$G(\mathbf{m}) = N_{ava} = a \exp\left[-\left(\frac{\Delta - b}{c}\right)^2\right], \quad (2)$$

where a is the amplitude of the distribution, b the distance of the peak amplitude and c the width of the distribution. While we do not have images just before and just after the event, we derived an estimation of the number of triggered avalanches from this relationship:

$$N_{ava} = \Delta n - \bar{q} \times n\Delta t/100, \quad (3)$$

where $\bar{q}$ is the long-term avalanche rate (i.e., we conservatively considered 6%.MYear^{-1}). Because the avalanche susceptibility is not evenly distributed (i.e., steep slopes only located inside impact craters, non-homogeneous surface/sub-surface properties), we only consider observations that meet the following criteria: $\Gamma^* < 1.93$, and $\Delta t < 1.5$ MYear, to only account for the lowest thermal inertia (see Fig. 3) and the smallest time span between images to reduce biases. Then, we used a Monte Carlo method to invert the most probable epicenter location using a maximum likelihood function with a Laplacian distribution of errors (Mosegaard and Tarantola, 1995) (See Supp. Info. Text S4). The resulting probability distribution of the epicenter under all of

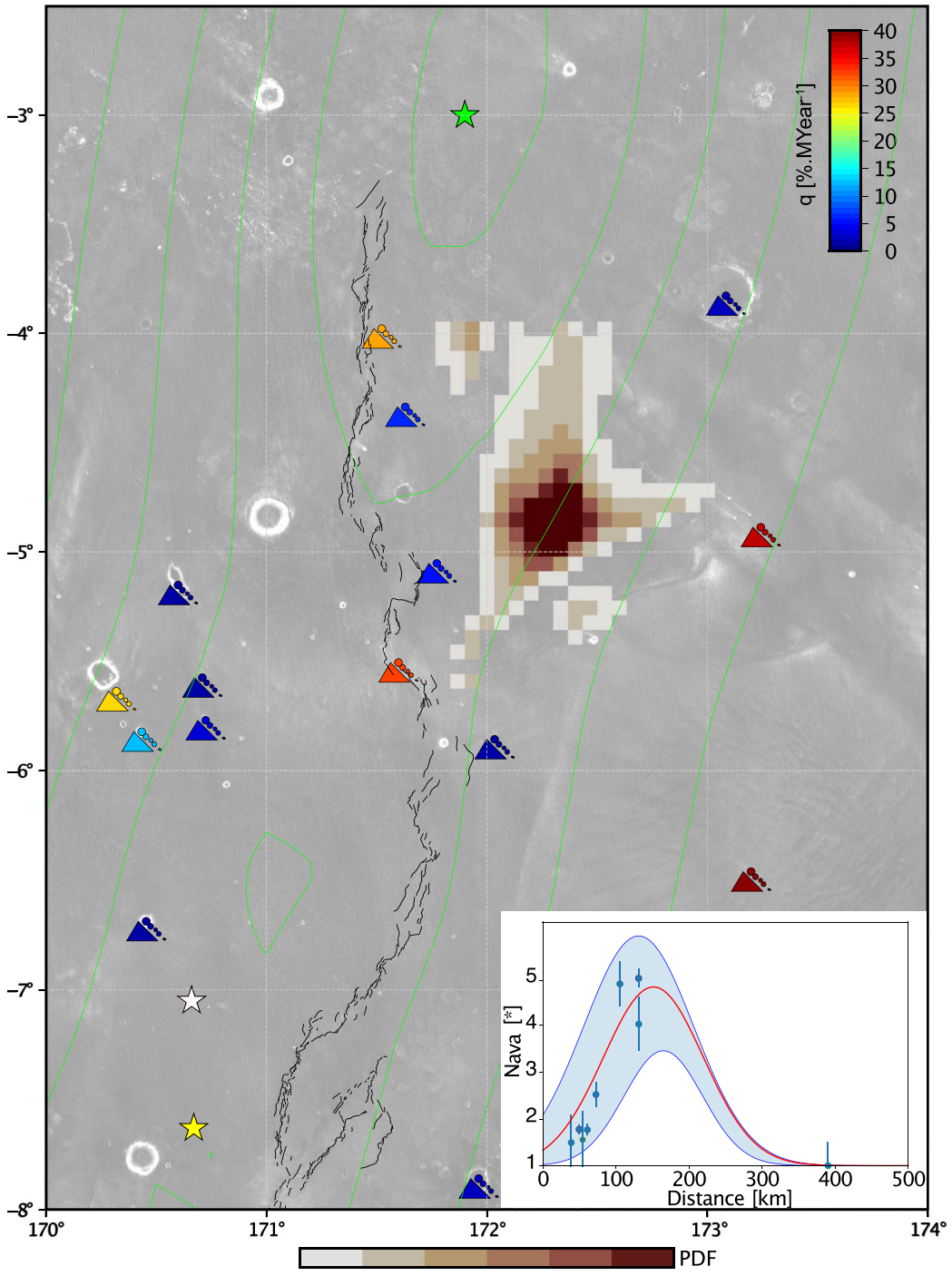

Fig. 5. Probability distribution of the epicenter inferred from avalanche observations (reddish colormap). Symbols show number of avalanches observed on post-event images. Color scales with the rate q. The green star (upper center) is the maximum peak of the estimated epicenter and its uncertainty ellipses (green contours) obtained from body waves (Kawamura et al., 2023), the white star, the location estimated from multi-orbit surface waves (Panning et al., 2023), and the yellow star is the estimated epicenter derived from the surface waves (Kim et al., 2022). Black lines are detailed surface traces of the main wrinkle ridge in the vicinity of the epicentral area. Background map is the thermal inertia Γ. (Inset) Expected avalanche density distribution with confidence interval from Monte Carlo inversion using Eq. (2) with respect to the number of avalanche N_{ava} derived from Eq. (3). (For interpretation of the references to color in this figure legend, the reader is referred to the web version of this article.)

these considerations is given in Fig. 5. It is situated in between the locations obtained from both body and surface waves analysis respectively (Kawamura et al., 2023; Panning et al., 2023; Kim et al., 2022), then included in the uncertainty ellipses of epicentral locations (green contours in Fig. 5).

This distribution can lead us to two different interpretations regarding the source mechanism of the quake, mainly related to internal tectonic activity. A first hypothesis would be based on the fact that our distribution is slightly shifted toward the East from the wrinkle ridges, on the flanks of Apollinaris Patera. It is now well supported that Mars still hosts remnant volcano-tectonic activity, especially along Cerberus Fossae (Giardini et al., 2020; Horvath et al., 2021; Perrin et al., 2022; Stähler et al., 2022), possibly due to the presence of a plume (Broquet and Andrews-Hanna, 2022), and associated with normal slip motion (Brinkman et al., 2021; Jacob et al., 2022). While the moment tensor analysis of the S1222a event can give very different

slip motions, NNW-SSE normal faulting is a possible solution (Maguire et al., 2023), highlighting a possible activity of Apollinaris Patera at depth. However, unlike Cerberus Fossae, Apollinaris Patera is an old Noachian volcano, thus it seems unlikely that remnant volcanic activity would be present at shallow depth. A second hypothesis would be related to the 450 km long wrinkle ridge, trending NNE-SSW, and cross-cutting the Hesperian terrains between the two epicentral locations (black lines in Fig. 5). The probability distribution of the epicenter inferred from the avalanche rate is about 30 to 60 km East of this major structure. The shape of the topographic profile across the ridge is an asymmetric arch-ridge, with a steep slope facing West and a shallow slope facing East (Fig. 1), which would imply a main East-dipping thrust at depth (Andrews-Hanna, 2020). Assuming a fault dip of 34° to 42° for arch-ridges (Andrews-Hanna, 2020), a probability distribution situated about 30 to 60 km East of the wrinkle ridge would lead to a hypocentral depth ranging from 20 to 54 km. This range of depth is in agreement with the best solutions found by Maguire et al. (2023). Along with another study by Brinkman et al. (2023), their preferred solutions present mainly reverse slip motions striking E-W to NW-SE, which is not optimally oriented with the overall wrinkle ridge observed from orbital imagery. However, local large variations in fault strikes are possible along a wrinkle ridge. Note that the wrinkle ridges are cross-cutting a large E-W bulge situated at about -5° latitude, connecting the flanks of Apollinaris Patera and a large crater in the west (Fig. 1). This bulge presents hundreds of meters of difference in elevation and slight apparent thermal inertia anomalies that could indicate a bedrock affected by an old tectonic structure. Interestingly, the bulge's azimuth is aligned with our probability distribution of the epicenter. More work would be needed to understand the origin of this structure and a possible link with the source of the marsquake.

It should also be noted that source locations obtained from other methods such as surface waves or coda characteristics give different locations (Kim et al., 2022; Panning et al., 2023; Menina et al., 2023). Both studies using surface waves predict source locations more toward the south as shown in 5. This is due to different back azimuth they obtained for surface waves compared from that described in Kawamura et al. (2023) using body waves. Panning et al. (2023) also discusses the possibility that the source location could be in the southern hemisphere. Interestingly, Menina et al. (2023) conclude that they need a thick (60 km) diffusive layer to explain the coda shape of S1222a. This could imply that either the source location could be in the highlands of the southern hemisphere (Wieczorek et al., 2022), or that thermal anomalies at depth are present in the Appollinaris area.

Our work leads us to propose that the source of the quake is likely due to thermal contraction due to Mars' cooling through time. The peak of thermal contraction and wrinkle ridge formation occurred during the early Hesperian and decreased progressively until now (Watters, 1993). Even if the wrinkle ridge in Fig. 5 is well expressed in morphology, its surface trace ends to the north, near the transition between Hesperian and Amazonian terrains (Tanaka et al., 2014). This indicates that the ridge has not been active in recent times. However, thermal contraction is still ongoing on Mars and might re-activate local mechanical weaknesses in the martian crust, such as wrinkle ridges, over larger recurrence time periods. If such activity is real, microseismicity should be associated with it.

4. Conclusions

In our comprehensive study of surface features surrounding the S1000a and S1222a seismic events on Mars, we utilized MRO orbital data to assess the associated avalanche rates. Our findings reveal a substantial increase in avalanches following the S1000a impact event, suggesting its indirect aftermaths, likely via secondary impacts. The S1222a event presented a more complex scenario, necessitating thorough investigation. We established pre-event avalanche rates in line with global estimates from Aharonson et al. (2003) and those near Olympus Mons obtained by Heyer et al. (2019), ranging between 1 and 6%.MYears^{-1}. These rates, when compared to post-event rates of up to 40%.MYear^{-1} near the estimated epicenter (Kawamura et al., 2023; Panning et al., 2023; Kim et al., 2022), underscore a significant increase in areas of lower apparent thermal inertia. This leads us to propose that the S1222a marsquake could be the driving factor behind the observed increase in avalanches. This analysis also enabled us to estimate a probable epicenter for the marsquake, considering the Γ^* threshold of 1.5 and a radial ground acceleration. This inferred location is intriguingly situated near a volcanic edifice and a North-South wrinkle ridge, highlighting the geological complexity of the region. Our study not only might suggest that current seismic activity on Mars can initiate mass wasting processes like dust avalanches but also opens avenues for exploring regions with observed avalanches and other seismic events detected by the InSight mission. The increased rates of avalanches in areas with historical seismic sources suggest that ground deformation plays a pivotal role in these phenomena. This methodology can be invaluable in future seismic event analyses, where visible aftermaths such as avalanches can offer significant insights into epicenter locations. Overall, our findings demonstrate that avalanches on Mars serve as a crucial tool for documenting rapid processes, from discrete surface perturbations like impacts to more continuous events like quakes. This understanding significantly enhances our ability to study and interpret the dynamic surface and subsurface processes of Mars

5. Open research

The orbital data are available online: HRSC are available at ESA's Planetary Science Archive (https://www.cosmos.esa.int/web/psa/mars-express). THEMIS data are available at Arizona State University's repository (https://themis.asu.edu). MOC images are available at the PDS Imaging Node (https://pds-imaging.jpl.nasa.gov/data/mgs-m-moc-na_wa-2-sdp-l0-v1.0/). MOLA data are available at the PDS Geosciences Node (https://pds-geosciences.wustl.edu/missions/mgs/mola.html). Apparent thermal inertia map is provided by the USGS (https://astrogeology.usgs.gov/maps/mars-themis-derived-global-thermal-inertia-mosaic). HiRISE data, including the post-event images, are available at the University of Arizona's dedicated website (https://www.uahirise.org). CTX image are available at the Imaging PDS Node (https://pds-imaging.jpl.nasa.gov/data/mro/mars_reconnaissance_orbiter/ctx/). The post-event CTX images will be posted on the NASA PDS by MSSS by the time of publication. Meanwhile, readers can have access to the mosaic at https://www.dropbox.com/sh/u1cykaotwxvi7ga/AAAsDcqw4FrkGDqjb4HTFmjka?dl=0. The avalanche catalogue is available on Zenodo (doi:10.5281/zenodo.7679315). The research data are available on the IPGP Research Collection (doi:10.18715/IPGP.2024.lr68kbwy) The InSight seismic event catalogue version 9 (InSight Marsquake Service, 2022) and waveform data (InSight Mars SEIS Data Service, 2019a,b) are available from the IPGP Datacenter and IRIS-DMC, as are previous catalogue versions. Seismic waveforms are also available from NASA PDS. The crustal thickness grid is available on Zenodo (doi:10.5281/zenodo.6477509).

CRediT authorship contribution statement

A. Lucas: Conceptualization, Data curation, Formal analysis, Investigation, Methodology, Resources, Validation, Visualization, Writing – original draft, Writing – review & editing. **I.J. Daubar:** Data curation, Funding acquisition, Methodology, Resources, Writing – original draft, Writing – review & editing. **M. Le Teuff:** Data curation, Formal analysis, Writing – review & editing. **C. Perrin:** Data curation, Investigation, Methodology, Resources, Validation, Writing – original draft, Writing – review & editing. **T. Kawamura:** Investigation, Writing – review & editing. **L. Posiolova:** Investigation, Resources, Writing – review & editing. **P. Lognonné:** Conceptualization, Funding acquisition, Writing – review

& editing. **S. Rodriguez:** Conceptualization, Writing – review & editing. **D. Giardini:** Writing – review & editing. **G. Sainton:** Methodology, Writing – review & editing. **A. Mangeney:** Writing – review & editing. **A. McEwen:** Resources, Writing – review & editing.

Declaration of competing interest

The authors declare that they have no known competing financial interests or personal relationships that could have appeared to influence the work reported in this paper.

Data availability

The data are available on the web through PDS, Zenodo and the IPGP Research Collection for which links are provided in the acknowledgment section.

Acknowledgments

Authors thank Menina S., Margerin L., Kim D., Malystskyy D., Stähler S., Wieczorek M., Panning M. for InSightful discussions on the S1222a event. Authors thank Dundas C.M. for his help in accessing the post-event HiRISE images for both events. The authors express their gratitude to Ferrari C. for providing valuable insights into thermal inertia, to A. Spiga for his expertise on the output of General Circulation Models (GCMs), and to P. Souloumiac for her expert knowledge on slope failure conditions. Authors thank anonymous reviewers and the associate editor for their constructive feedback that substantially improved the manuscript. All authors declare no conflict of interest. French co-authors acknowledge the French Space Agency CNES and ANR (ANR-19-CE31-0008). AL, TK, PL, SR, GS, AM acknowledge Idex Paris Cité (ANR-18-IDEX-0001). IJD was funded by NASA, United States InSight PSP grant 80NSSC20K0971.

Appendix A. Supplementary data

Supplementary material related to this article can be found online at https://doi.org/10.1016/j.icarus.2023.115942.

References

Aharonson, O., Schorghofer, N., Gerstell, M.F., 2003. Slope streak formation and dust deposition rates on Mars: Martian slope streak formation rates. J. Geophys. Res.: Planets 108 (E12), http://dx.doi.org/10.1029/2003JE002123, Retrieved 2022-07-14, from http://doi.wiley.com/10.1029/2003JE002123.

Andrews-Hanna, J.C., 2020. The tectonic architecture of wrinkle ridges on Mars. Icarus 351 (October 2019), 113937. http://dx.doi.org/10.1016/j.icarus.2020.113937, Retrieved from http://dx.doi.org/10.1016/j.icarus.2020.113937.

Banerdt, W.B., Smrekar, S.E., Banfield, D., Giardini, D., Golombek, M., Johnson, C.L., et al., 2020. Initial results from the InSight mission on Mars. Nat. Geosci. 13 (3), 183–189.

Baratoux, D., Mangold, N., Forget, F., Cord, A., Pinet, P., Daydou, Y., et al., 2006. The role of the wind-transported dust in slope streaks activity: Evidence from the HRSC data. Icarus 183 (1), 30–45. http://dx.doi.org/10.1016/j.icarus.2006.01.023.

Battalio, M., Wang, H., 2021. The Mars Dust Activity Database (MDAD): A comprehensive statistical study of dust storm sequences. Icarus 354, 114059. http://dx.doi.org/10.1016/j.icarus.2020.114059, Retrieved from https://linkinghub.elsevier.com/retrieve/pii/S001910352030405X.

Bergonio, J.R., Rottas, K.M., Schorghofer, N., 2013. Properties of martian slope streak populations. Icarus 225 (1), 194–199. http://dx.doi.org/10.1016/j.icarus.2013.03.023, Retrieved from https://www.sciencedirect.com/science/article/pii/S0019103513001395.

Bhardwaj, A., Sam, L., Martín-Torres, F.J., Zorzano, M.-P., 2019. Are slope streaks indicative of global-scale aqueous processes on contemporary mars? Rev. Geophys. 57 (1), 48–77. http://dx.doi.org/10.1029/2018RG000617.

Bhardwaj, A., Sam, L., Martín-Torres, F.J., Zorzano, M.-P., Fonseca, R.M., 2017. Martian slope streaks as plausible indicators of transient water activity. Sci. Rep. 7 (1), 7074. http://dx.doi.org/10.1038/s41598-017-07453-9, Retrieved from http://dx.doi.org/10.1038/s41598-017-07453-9.

Bontemps, N., Lacroix, P., Larose, E., Jara, J., Taipe, E., 2020. Rain and small earthquakes maintain a slow-moving landslide in a persistent critical state. Nature Commun. 11 (1), 780.

Böse, M., Stähler, S.C., Deichmann, N., Giardini, D., Clinton, J., Lognonné, P., et al., 2021. Magnitude scales for marsquakes calibrated from InSight data. Bull. Seismol. Soc. Am. 111 (6), 3003–3015.

Brinkman, N., Sollberger, D., Schmelzbach, C., Stähler, S.C., Robertsson, J., 2023. Applications of time-frequency domain polarization filtering to InSight seismic data. Earth Space Sci. 10 (11), e2023EA003169.

Brinkman, N., Stähler, S.C., Giardini, D., Schmelzbach, C., Khan, A., Jacob, A., et al., 2021. First focal mechanisms of marsquakes. J. Geophys. Res.: Planets http://dx.doi.org/10.1029/2020JE006546, Retrieved from https://agupubs.onlinelibrary.wiley.com/doi/abs/10.1029/2020JE006546.

Broquet, A., Andrews-Hanna, J.C., 2022. Geophysical evidence for an active mantle plume underneath Elysium Planitia on Mars. Nat. Astron. http://dx.doi.org/10.1038/s41550-022-01836-3.

Brown, J., Roberts, G., 2019. Possible evidence for variation in magnitude for marsquakes from fallen boulder populations, Grjota Valles, Mars. J. Geophys. Res. Planets 124 (3), 801–812. http://dx.doi.org/10.1029/2018JE005622.

Burleigh, K.J., Melosh, H.J., Tornabene, L.L., Ivanov, B., McEwen, A.S., Daubar, I.J., 2012. Impact airblast triggers dust avalanches on mars. Icarus 217 (1), 194–201.

Ceylan, S., Clinton, J.F., Giardini, D., Stähler, S.C., Horleston, A., Kawamura, T., et al., 2022. The marsquake catalogue from InSight, sols 0–1011. Phys. Earth Planet. Inter. 333, 106943.

Chen, X.-l., Shan, X., Wang, M.-m., Liu, C.-g., Han, N.-n., 2020. Distribution pattern of coseismic landslides triggered by the 2017 jiuzhaigou ms 7.0 earthquake of China: Control of seismic landslide susceptibility. ISPRS Int. J. Geo-Inf. 9, 198. http://dx.doi.org/10.3390/ijgi9040198.

Christensen, P.R., Bandfield, J.L., Hamilton, V.E., Ruff, S.W., Kieffer, H.H., Titus, T.N., et al., 2001. Mars Global Surveyor Thermal Emission Spectrometer experiment: Investigation description and surface science results. J. Geophys. Res.: Planets 106 (E10), 23823–23871.

Christensen, P.R., Jakosky, B.M., Kieffer, H.H., Malin, M.C., Jr., H.Y.M., Nealson, K., et al., 2004. The thermal emission imaging system (themis) for the mars 2001 odyssey mission. In: Russell, C.T. (Ed.), 2001 Mars Odyssey. Springer Netherlands, Dordrecht, pp. 85–130.

Chuang, F.C., Beyer, R.A., McEwen, A.S., Thomson, B.J., 2007. HiRISE observations of slope streaks on Mars. Geophys. Res. Lett. 34 (20), http://dx.doi.org/10.1029/2007GL031111, Retrieved from https://agupubs.onlinelibrary.wiley.com/doi/abs/10.1029/2007GL031111.

Clinton, J.F., Ceylan, S., van Driel, M., Giardini, D., Stähler, S.C., Böse, M., et al., 2021. The Marsquake catalogue from InSight, sols 0–478. Phys. Earth Planet. Inter. 310, 106595.

Davison, A.C., Hinkley, D.V., 1997. Bootstrap Methods and their Application. Cambridge University Press.

Dundas, C.M., 2020. Geomorphological evidence for a dry dust avalanche origin of slope streaks on Mars. Nat. Geosci. 13 (7), 473–476. http://dx.doi.org/10.1038/s41561-020-0598-x, Retrieved from http://dx.doi.org/10.1038/s41561-020-0598-x.

Durand, V., Mangeney, A., Bernard, P., Jia, X., Bonilla, F., Satriano, C., Saurel, J.-M., Aissaoui, E.M., Peltier, A., Ferrazzini, V., Kowalski, P., Lauret, F., Brunet, C., Hibert, C., 2023. Repetitive small seismicity coupled with rainfall can trigger large slope instabilities on metastable volcanic edifices. Communications Earth & Environment 4 (1), 383. http://dx.doi.org/10.1038/s43247-023-00996-y, https://doi.org/10.1038/s43247-023-00996-y.

Efron, B., Tibshirani, R.J., 1993. An Introduction To the Bootstrap. CRC Press.

Fergason, R.L., Christensen, P.R., Kieffer, H.H., 2006. High-resolution thermal inertia derived from the Thermal Emission Imaging System (THEMIS): Thermal model and applications. J. Geophys. Res.: Planets 111 (E12), http://dx.doi.org/10.1029/2006JE002735, Retrieved from http://doi.wiley.com/10.1029/2006JE002735.

Ferguson, H.M., Lucchitta, B.K., 1984. Dark streaks on talus slopes, Mars. In: NASA. Washington Rept. of Planetary Geol. Programs. pp. 188–190, (SEE N84-23431 13-91).

Fernando, B., Daubar, I.J., Charalambous, C., Grindrod, P.M., Stott, A., Al Ateqi, A., et al., 2023. A tectonic origin for the largest marsquake observed by InSight. Geophys. Res. Lett. 50, 1–10. http://dx.doi.org/10.1029/2023GL103619.

Ferris, J.C., Dohm, J.M., Baker, V.R., Maddock III, T., 2002. Dark slope streaks on Mars: Are aqueous processes involved? Geophys. Res. Lett. 29 (10), 128–1–128–4. http://dx.doi.org/10.1029/2002GL014936, Retrieved from https://agupubs.onlinelibrary.wiley.com/doi/abs/10.1029/2002GL014936.

Gerstell, M.F., Aharonson, O., Schorghofer, N., 2004. A distinct class of avalanche scars on Mars. Icarus 168 (1), 122–130. http://dx.doi.org/10.1016/j.icarus.2003.11.005, Retrieved from https://linkinghub.elsevier.com/retrieve/pii/S0019103503003907.

Giardini, D., Lognonné, P., Banerdt, W., Pike, W., Christensen, U., Ceylan, S., et al., 2020. The Seismicity of Mars. Nat. Geosci. 13 (3), 205–212. http://dx.doi.org/10.1038/s41561-020-0539-8.

Head, J.W., Marchant, D.R., Dickson, J.L., Levy, J.S., Morgan, G.A., 2007. Slope streaks in the antarctic dry valleys: Characteristics, candidate formation mechanisms, and implications for slope streak formation in the martian environment. In: 38th Annual Lunar and Planetary Science Conference. In: Lunar and Planetary Science Conference, p. 1935.

Heyer, T., Kreslavsky, M., Hiesinger, H., Reiss, D., Bernhardt, H., Jaumann, R., 2019. Seasonal formation rates of martian slope streaks. Icarus 323, 76–86. http://dx.doi.org/10.1016/j.icarus.2019.01.010, Retrieved from https://linkinghub.elsevier.com/retrieve/pii/S0019103518306857.

Heyer, T., Raack, J., Hiesinger, H., Jaumann, R., 2020. Dust devil triggering of slope streaks on Mars. Icarus 351, 113951. http://dx.doi.org/10.1016/j.icarus.2020.113951, Retrieved from https://www.sciencedirect.com/science/article/pii/S0019103520303249.

Horvath, D.G., Moitra, P., Hamilton, C.W., Craddock, R.A., Andrews-Hanna, J.C., 2021. Evidence for geologically recent explosive volcanism in Elysium Planitia, Mars. Icarus 365, 114499. http://dx.doi.org/10.1016/j.icarus.2021.114499.

InSight Marsquake Service, 2022. Mars seismic catalogue, InSight mission; V12 2022-10-01. http://dx.doi.org/10.12686/a18, Retrieved from https://www.insight.ethz.ch/seismicity/catalog/v12.

Jacob, A., Plasman, M., Perrin, C., Fuji, N., Lognonné, P., Xu, Z., et al., 2022. Seismic sources of InSight marsquakes and seismotectonic context of Elysium Planitia, Mars. Tectonophysics 837, 229434. http://dx.doi.org/10.1016/j.tecto.2022.229434, Retrieved from https://www.sciencedirect.com/science/article/pii/S0040195122002281.

Kawamura, T., Clinton, J., Zenhäusern, G., Ceylan, S., Horleston, A., Dahmen, N., et al., 2023. S1222a - the largest Marsquake detected by InSight. Geophys. Res. Lett. http://dx.doi.org/10.1029/2022GL101543.

Kim, D., Stähler, S.C., Ceylan, S., Lekic, V., Maguire, R., Zenhäusern, G., et al., 2022. Structure along the martian dichotomy constrained by Rayleigh and Love waves and their overtones. Geophys. Res. Lett. e2022GL101666.

Knapmeyer, M., Oberst, J., Hauber, E., Wählisch, M., Deuchler, C., Wagner, R., 2006. Working models for spatial distribution and level of Mars' seismicity. J. Geophys. Res. E Planets 111 (11), 1–23. http://dx.doi.org/10.1029/2006JE002708.

Knapmeyer, M., Stähler, S., Plesa, A.-C., Ceylan, S., Charalambous, C., Clinton, J., et al., 2023. The global seismic moment rate of mars after event S1222a. Geophys. Res. Lett. 50 (7), e2022GL102296.

Kreslavsky, M.A., Head, J.W., 2009. Slope streaks on Mars: A new "wet" mechanism. Icarus 201 (2), 517–527. http://dx.doi.org/10.1016/j.icarus.2009.01.026, Retrieved from https://linkinghub.elsevier.com/retrieve/pii/S0019103509000608.

Livio, F., Ferrario, M.F., 2020. Assessment of attenuation regressions for earthquake-triggered landslides in the Italian Apennines: InSights from recent and historical events. Landslides 17 (12), 2825–2836.

Lognonné, P., Banerdt, W.B., Giardini, D., Pike, W.T., Christensen, U., Laudet, P., et al., 2019. SEIS: Insight's seismic experiment for internal structure of Mars. Space Sci. Rev. 215 (1), 12. http://dx.doi.org/10.1007/s11214-018-0574-6, Retrieved from http://dx.doi.org/10.1007/s11214-018-0574-6 http://link.springer.com/10.1007/s11214-018-0574-6.

Lombardo, L., Tanyas, H., 2022. From scenario-based seismic hazard to scenario-based landslide hazard: fast-forwarding to the future via statistical simulations. Stoch. Environ. Res. Risk Assess 36, 2229–2242.

Lucas, A., 2010. Dynamique des instabilités gravitaires par modélisation et télédétection: Applications aux exemples martiens (Theses). Institut de physique du globe de paris - IPGP, Retrieved from https://tel.archives-ouvertes.fr/tel-00503212.

Lucas, A., Mangeney, A., 2007. Mobility and topographic effects for large valles marineris landslides on mars. Geophys. Res. Lett. 34 (10).

Lucas, A., Mangeney, A., Ampuero, J.P., 2014. Frictional velocity-weakening in landslides on Earth and on other planetary bodies. Nature Commun. 5 (1), 3417.

Lucas, A., Mangeney, A., Mège, D., Bouchut, F., 2011. Influence of the scar geometry on landslide dynamics and deposits: Application to Martian landslides. J. Geophys. Res.: Planets 116 (E10).

Maguire, R., Lekić, V., Kim, D., Schmerr, N., Li, J., Beghein, C., Huang, Q., Irving, J.C.E., Karakostas, F., Lognonné, P., Stähler, S.C., Banerdt, W.B., 2023. Focal mechanism determination of event s1222a and implications for tectonics near the dichotomy boundary in southern elysium planitia, mars. Journal of Geophysical Research: Planets 128 (9), e2023JE007793, http://dx.doi.org/10.1029/2023JE007793.

Malin, M.C., Bell, J.F., Cantor, B.A., Caplinger, M.A., Calvin, W.M., Clancy, R.T., et al., 2007. Context camera investigation on board the Mars reconnaissance orbiter. J. Geophys. Res. 112 (E5), E05S04. http://dx.doi.org/10.1029/2006JE002808, Retrieved from http://doi.wiley.com/10.1029/2006JE002808.

Malin, M.C., Danielson, G.E., Ingersoll, A.P., Masursky, H., Veverka, J., Ravine, M.A., Soulanille, T.A., 1992. Mars observer camera. J. Geophys. Res.: Planets 97 (E5), 7699–7718.

Martino, S., Fiorucci, M., Marmoni, G.M., Casaburi, L., Antonielli, B., Mazzanti, P., 2022. Increase in landslide activity after a low-magnitude earthquake as inferred from DInSAR interferometry. Sci. Rep. 12 (1), 2686.

McEwen, A.S., Eliason, E.M., Bergstrom, J.W., Bridges, N.T., Hansen, C.J., Delamere, W.A., et al., 2007. Mars reconnaissance orbiter's high resolution imaging science experiment (HiRISE). J. Geophys. Res. 112 (E5), E05S02. http://dx.doi.org/10.1029/2005JE002605, Retrieved from http://doi.wiley.com/10.1029/2005JE002605.

Menina, S., Margerin, L., Kawamura, T., Heller, G., Drilleau, M., Xu, Z., et al., 2023. Stratification of heterogeneity in the lithosphere of Mars from envelope modeling of event S1222a and near impacts: Interpretation and implications for very-high-frequency events. Geophys. Res. Lett. 50 (7), e2023GL103202.

Miyamoto, H., 2004. Fluid dynamical implications of anastomosing slope streaks on Mars. J. Geophys. Res. 109 (E6), E06008. http://dx.doi.org/10.1029/2003JE002234, Retrieved 2022-07-14, from http://doi.wiley.com/10.1029/2003JE002234.

Mosegaard, K., Tarantola, A., 1995. Monte Carlo sampling of solutions to inverse problems. J. Geophys. Res.: Solid Earth 100 (B7), 12431–12447. http://dx.doi.org/10.1029/94JB03097.

Neukum, G., Jaumann, R., 2004. The high resolution stereo camera of Mars express. ESA Special Publ. 1240, 1–19.

Panning, M.P., Banerdt, W.B., Beghein, C., Carrasco, S., Ceylan, S., Clinton, J.F., et al., 2023. Locating the largest event observed on mars with multi-orbit surface waves. Geophys. Res. Lett. 50 (1), e2022GL101270.

Perrin, C., Jacob, A., Lucas, A., Myhill, R., Hauber, E., Batov, A., et al., 2022. Geometry and segmentation of cerberus fossae, Mars: Implications for marsquake properties. J. Geophys. Res.: Planets 127 (1), http://dx.doi.org/10.1029/2021JE007118, e2021JE007118.

Phillips, C.B., Burr, D.M., Beyer, R.A., 2007. Mass movement within a slope streak on Mars. Geophys. Res. Lett. 34 (21), http://dx.doi.org/10.1029/2007GL031577, Retrieved from https://agupubs.onlinelibrary.wiley.com/doi/abs/10.1029/2007GL031577.

Posiolova, L.V., Lognonné, P., Banerdt, W.B., Clinton, J., Collins, G.S., Kawamura, T., et al., 2022. Largest recent impact craters on Mars: Orbital imaging and surface seismic co-investigation. Science 378 (6618), 412–417.

Roberts, G.P., Matthews, B., Bristow, C., Guerrieri, L., Vetterlein, J., 2012. Possible evidence of paleomarsquakes from fallen boulder populations, Cerberus Fossae, Mars. J. Geophys. Res. Planets 117 (E2), n/a–n/a. http://dx.doi.org/10.1029/2011JE003816.

Rosser, N., Kincey, M., Oven, K., Densmore, A., Robinson, T., Pujara, D.S., et al., 2021. Changing significance of landslide Hazard and risk after the 2015 Mw 7.8 Gorkha, Nepal Earthquake. Prog. Disaster Sci. 10, 100159.

Schorghofer, N., Aharonson, O., Gerstell, M., Tatsumi, L., 2007. Three decades of slope streak activity on Mars. Icarus 191 (1), 132–140. http://dx.doi.org/10.1016/j.icarus.2007.04.026, Retrieved from https://www.sciencedirect.com/science/article/pii/S0019103507001960.

Schorghofer, N., Aharonson, O., Khatiwala, S., 2002. Slope streaks on Mars: Correlations with surface properties and the potential role of water: Slope streaks on Mars. Geophys. Res. Lett. 29 (23), 41–1–41–4. http://dx.doi.org/10.1029/2002GL015889, Retrieved 2022-07-14, from http://doi.wiley.com/10.1029/2002GL015889.

Schorghofer, N., King, C.M., 2011. Sporadic formation of slope streaks on Mars. Icarus 216 (1), 159–168. http://dx.doi.org/10.1016/j.icarus.2011.08.028, Retrieved from https://linkinghub.elsevier.com/retrieve/pii/S0019103511003459.

Smith, D.E., Zuber, M.T., Frey, H.V., Garvin, J.B., Head, J.W., Muhleman, D.O., et al., 2001. Mars Orbiter Laser Altimeter: Experiment summary after the first year of global mapping of Mars. J. Geophys. Res.: Planets 106 (E10), 23689–23722.

Stähler, S.C., Mittelholz, A., Perrin, C., Kawamura, T., Kim, D., Knapmeyer, M., et al., 2022. Tectonics of Cerberus Fossae unveiled by marsquakes. Nat. Astron. 6 (12), 1376–1386. http://dx.doi.org/10.1038/s41550-022-01803-y.

Sullivan, R., Thomas, P., Veverka, J., Malin, M., Edgett, K.S., 2001. Mass movement slope streaks imaged by the Mars Orbiter Camera. J. Geophys. Res.: Planets 106 (E10), 23607–23633. http://dx.doi.org/10.1029/2000JE001296.

Tanaka, K., Skinner, J., Jr., D., J.M., I., Kolb, E., Fortezzo, C., et al., 2014. Geologic map of mars. U.S. Geological Survey Scientific pamphlet 43 p., http://dx.doi.org/10.3133/sim3292.

Tatard, L., 2010. Statistical analysis of triggered landslides : implications for earthquake and weather controls (Ph.D. thesis). University of Canterbury and Université de Grenoble.

Valantinas, A., Becerra, P., Pommerol, A., Tornabene, L., Affolter, L., Cremonese, G., et al., 2021. CaSSIS color and multi-angular observations of Martian slope streaks. Planet. Space Sci. 209, 105373. http://dx.doi.org/10.1016/j.pss.2021.105373, Retrieved from https://linkinghub.elsevier.com/retrieve/pii/S0032063321002129.

Watters, T.R., 1993. Compressional tectonism on Mars. J. Geophys. Res. 98 (E9), 17049. http://dx.doi.org/10.1029/93JE01138, Retrieved from http://doi.wiley.com/10.1029/93JE01138.

Wieczorek, M.A., Broquet, A., McLennan, S.M., Rivoldini, A., Golombek, M., Antonangeli, D., et al., 2022. Insight constraints on the global character of the martian crust. J. Geophys. Res.: Planets 127 (5), e2022JE007298.